buildings

MDPI

Article

Mayfly–Deep Learning Fusion for High-Dimensional Parameter Identification and Reinforcement of Historical Buildings

Zhong Peng [1], Bin Cheng [1], Shanjun Zhang [1,*], Zhiyong Li [2] and Wei Li [3]

[1] School of Engineering and Architecture, Wuhan City Polytechnic, Wuhan 430064, China; pengzhong@whcp.edu.cn (Z.P.)
[2] School of Civil Engineering and Architecture, Wuhan University of Technology, Wuhan 430070, China
[3] School of Computer Science, Wuhan City Polytechnic, Wuhan 430064, China
* Correspondence: 02002038@whcp.edu.cn

Abstract

Structural health assessment of historic buildings frequently relies on finite element (FE) model updating, yet high-dimensional parameter identification under sparse, noise-contaminated modal data can reduce robustness and lead to prohibitive computational cost. This paper proposes an application-oriented integrated workflow that improves identification stability while accelerating the updating process. A multi-indicator objective function is formulated by combining residuals of natural frequencies and mode shapes with sensitivity-based consistency relations. The inverse problem is solved using the Mayfly Algorithm (MA), and a deep neural network (DNN) surrogate is introduced to replace repeated FE modal analyses during the optimization, thereby reducing the overall computational burden. The proposed workflow is demonstrated on the Christian Lutheran Church in Wuhan, China, constructed from 1923 to 1924, using operational modal testing data collected at 25 measurement points. A refined FE model is updated by identifying 24 grouped stiffness reduction coefficients that represent columns, beams, walls, and slabs across different floors. The updated model shows substantially improved agreement with the measured first four natural frequencies and corresponding mode shapes, enabling a quantitative diagnosis of stiffness degradation and supporting stiffness-oriented reinforcement planning. A stiffness enhancement target of 20% is adopted to guide intervention measures, and an analytical modal enhancement check is provided to relate the stiffness target to the expected frequency gain. The workflow offers a reproducible route for data-informed decision support in heritage building assessment and rehabilitation, while uncertainty quantification and post-intervention validation are identified as key priorities for future work. Under the available sparse modal information, the inverse problem is underdetermined; therefore, the reported stiffness-reduction coefficients should be interpreted as non-unique grouped solutions affected by modelling and measurement uncertainty, and the reinforcement measures are presented only as planning-level design proposals requiring post-intervention verification.

Keywords: historical buildings; high-dimensional parameter identification; dynamic stiffness; Mayfly algorithm; multi-indicator

Check for updates

Academic Editor: Dan Bompa

Received: 31 December 2025
Revised: 7 April 2026
Accepted: 10 April 2026
Published: 11 May 2026

Copyright: © 2026 by the authors. Licensee MDPI, Basel, Switzerland. This article is an open access article distributed under the terms and conditions of the Creative Commons Attribution (CC BY) license.

1. Introduction

As an essential component of cultural heritage, historical monuments not only serve as witnesses to human civilization but also provide crucial platforms for studying ancient

architectural techniques and cultural evolution [1,2]. Over time, environmental changes and natural aging have led to varying degrees of degradation, damage, and structural issues in these buildings, posing significant challenges to their long-term preservation [3–7]. Therefore, the development of scientifically effective protection and restoration methods is imperative [8–10]. Structural Health Monitoring (SHM) is a fundamental prerequisite for heritage conservation, playing a vital role in providing critical information for structural condition assessment and repair decision-making [11–15].

In the field of cultural heritage preservation, global researchers have conducted extensive studies aimed at achieving precise monitoring and scientific restoration through advanced technologies. Early research primarily focused on the foundational theories and traditional methods of heritage conservation [16–20]. In recent years, significant advancements in structural health monitoring have established it as a cornerstone of cultural heritage protection [21–31]. By collecting and analyzing data in real-time, SHM provides important support for structural condition assessment and the formulation of repair strategies. For instance, Song et al. (2018) [32] investigated the application of finite element model updating in damage identification of a century-old two-story reinforced concrete building. By analyzing vibration data and laser scanning, the study demonstrated that finite element model updating effectively identifies the existence, location, and extent of structural damage. The research emphasized the importance of environmental excitation and forced vibration testing, validating the model's accuracy through controlled damage experiments on the building's facade. Similarly, Nozari et al. (2017) [33] conducted a damage identification study on a 110-year-old ten-story reinforced concrete structure. The authors first established the baseline state of the building using modal testing data, then induced damage by removing external infill walls, employing operational modal analysis to identify changes in natural frequencies and mode shapes. The results indicated significant differences in updated model parameters across different datasets, with damage identification results highly consistent with actual conditions. Ramos et al. (2013) [34] conducted a comprehensive study on the dynamic structural health monitoring of the San Torcato Church. Through global dynamic identification analysis, the researchers implemented both static and dynamic monitoring systems to evaluate the effectiveness of structural interventions. This study highlighted the importance of using manual and robust optimization programs for modal parameter estimation, demonstrating the value of dynamic monitoring in tracking structural damage progression. Wu et al. (2024) [35] proposed a method for health detection and wind safety assessment of ancient residential buildings based on laser point clouds. Utilizing high-precision 3D laser scanning, the researchers assessed structural deformation and damage under typhoon conditions, confirming the method's effectiveness in detecting structural health indicators and providing reliable evidence for the protection of ancient buildings. Soleymani et al. (2023) [36] conducted a systematic review exploring damage detection and structural health monitoring technologies for masonry structures. The study emphasized that SHM systems can monitor key indicators such as acceleration, displacement, and stress, enhancing the assessment of masonry structures' health status through comprehensive measurement and analysis techniques. The authors advocated for the integration of multiple detection methods to address challenges related to hidden defects and maintenance costs.

Despite significant progress in damage identification and structural health monitoring in recent years, existing research methods still face numerous challenges and limitations. Traditional approaches primarily rely on single indicators or empirical models, making it difficult to effectively address the complexities of high-dimensional data environments, leading to significant constraints on parameter identification accuracy and efficiency. Current technologies exhibit notable deficiencies in handling the complexities of building

structures: firstly, they struggle to comprehensively consider critical parameters; secondly, they have weak multi-scale analysis capabilities; and thirdly, traditional optimization methods often face limitations in high-dimensional parameter identification, failing to fully exploit the inherent potential of dynamic building characteristics. More critically, current reinforcement schemes largely depend on engineers' experience, lacking a scientific quantitative assessment benchmark, which hinders accurate prediction and evaluation of reinforcement effects, severely limiting the scientific basis and specificity of the schemes.

Among existing alternatives, Bayesian model updating and related probabilistic inference frameworks provide a rigorous way to quantify parameter uncertainty and to incorporate prior information [24–31]. Those approaches are highly valuable, especially when repeated measurements and well-characterized noise models are available [37,38]. In the present heritage-building case, however, only a limited set of modal quantities was available and the main objective was to obtain a transparent deterministic baseline for engineering decision support. The proposed workflow should therefore be viewed as complementary to Bayesian updating rather than as a replacement for it.

To address these practical challenges, this study develops an application-oriented workflow that combines modal residuals, sensitivity relations, population-based optimization, and surrogate modeling for the FE updating of a historical building. The Mayfly Algorithm (MA) is used as the search engine for the grouped-parameter inverse problem, while the DNN surrogate is introduced only to reduce repeated FE evaluations. The intention is not to claim a fundamentally new updating theory, but to demonstrate how established techniques can be integrated into a workable engineering pipeline for condition assessment and rehabilitation planning under limited field data.

The main contributions of this study are as follows: (1) A multi-indicator objective function is formulated by combining frequency residuals, mode-shape residuals, and a weak prior response constraint to improve robustness under sparse modal information. (2) A DNN surrogate is combined with the MA optimizer to reduce the computational burden of searching a 24-parameter grouped space. (3) The identified grouped coefficients are used in a representative heritage-building case study to support the prioritization of candidate reinforcement measures. Accordingly, the contribution of this study is best understood as an engineering case demonstration of an integrated workflow, rather than a head-to-head methodological benchmark against probabilistic or Bayesian updating approaches.

Scope and limitations: This study reports a single case study and provides deterministic point estimates of grouped stiffness-reduction coefficients. The identified values represent effective parameters at the group level and may not be unique, because different parameter combinations can produce similar modal responses under sparse measurements. In addition, no direct comparison with Bayesian updating or other uncertainty-aware alternatives is carried out here; instead, those methods are regarded as complementary options for future work when richer modal data, repeat measurements, and explicit noise models are available. Section 2.5 discusses identifiability and uncertainty, while Section 3.7 outlines the required post-reinforcement verification procedure.

The remainder of this paper is organized as follows. Section 2 presents the multi-indicator objective function, model-reduction method, MA optimizer, DNN surrogate model, and identifiability considerations. Section 3 describes the case study of the Christian Lutheran Church Building, including the FE model, modal testing, parameter identification, and reinforcement planning. Section 4 concludes the paper.

2. Integrated Parameter Identification Workflow

2.1. Multi-Indicator Objective Function

Given the complexity of building structures and the large number of parameters involved, relying on a single metric for structural parameter identification may result in overlooking critical parameters. To address this limitation, a multi-indicator approach is proposed for structural parameter identification. Initially, the first-order sensitivity equation for the structural mode is introduced. For a structure with N degrees of freedom (DOF), the eigenvalue equation for undamped vibration can be expressed as

$$\mathbf{K}\mathbf{f}_i = \lambda_i \mathbf{M}\mathbf{f}_i \ , \ (i = 1, \ \ldots, \ p) \tag{1}$$

where $\mathbf{K}$ and $\mathbf{M}$ are the initial stiffness and mass matrices of the structure, respectively; λ_i and $\mathbf{f}_i$ denote the i-th eigenvalue and the corresponding eigenvector (mode shape) of the initial model, and p is the number of calculated modes. For most civil engineering structures, the mass matrix is commonly treated as constant during service, whereas deterioration and material degradation are mainly reflected by changes in the stiffness matrix. Therefore, if the mechanical parameters of the actual structure deviate from the initial assumptions, the characteristic equation can be rewritten using the updated stiffness matrix:

$$\mathbf{K}^*\mathbf{f}_i^* = \lambda_i^*\mathbf{M}\mathbf{f}_i^* \tag{2}$$

where λ_i^* and $\mathbf{f}_i^*$ represent the i-th eigenpair of the current (possibly damaged) structure, and $\mathbf{K}^*$ is the stiffness matrix of the actual structure. In a parametric FE model, $\mathbf{K}^*$ can be expressed as a linear combination of elemental (or regional) stiffness matrices scaled by reduction coefficients as follows:

$$\mathbf{K}^* = \mathbf{K} + \sum_{n=1}^{N_e} \alpha_n \mathbf{K}_n \ , \ (n = 1, \ \ldots, \ N_\mathrm{e}) \tag{3}$$

where N_e is the number of updating parameters, and $\mathbf{K}_n$ denotes the elemental/regional stiffness matrix associated with the n-th parameter in the initial model. The scalar α_n is the stiffness-reduction coefficient of the n-th parameter ($\alpha_n < 0$ indicates stiffness loss), and the vector $\alpha = [\alpha_1, \alpha_2, \ldots, \alpha_{Ne}]^T$ collects all reduction coefficients.

The first-order sensitivity of the i-th order eigenvalues and eigenvectors (mode shapes) with respect to the reduction coefficients α_n can be calculated using the following formulas [39]:

$$\frac{\partial \lambda_i}{\partial \alpha_n} = -\mathbf{f}_i^T \mathbf{K}_n \mathbf{f}_i \tag{4}$$

$$\frac{\partial \mathbf{f}_i}{\partial \alpha_n} = \sum_{k=1, k\neq i}^{N_e} \frac{\mathbf{f}_k^T \mathbf{K}_n \mathbf{f}_i \mathbf{f}_k}{\lambda_k - \lambda_i} \tag{5}$$

From this, the first-order sensitivity equation for the structural eigenvalues and mode shapes to the structural reduction coefficient can be written:

$$\begin{bmatrix} \frac{\partial \lambda_1}{\partial \alpha_n} & \cdots & \frac{\partial \lambda_1}{\partial \alpha_{N_e}} \\ \vdots & \ddots & \vdots \\ \frac{\partial \lambda_m}{\partial \alpha_n} & \cdots & \frac{\partial \lambda_m}{\partial \alpha_{N_e}} \\ \frac{\partial \mathbf{f}_1}{\partial \alpha_n} & \cdots & \frac{\partial \mathbf{f}_1}{\partial \alpha_{N_e}} \\ \vdots & \ddots & \vdots \\ \frac{\partial \mathbf{f}_l}{\partial \alpha_n} & \cdots & \frac{\partial \mathbf{f}_l}{\partial \alpha_{N_e}} \end{bmatrix} \boldsymbol{\alpha} = \mathbf{S}\boldsymbol{\alpha} \approx \Delta\Gamma = \begin{pmatrix} \Delta\Gamma_\lambda \\ \Delta\Gamma_\mathbf{f} \end{pmatrix} \tag{6}$$

Let $\Delta\Gamma_\lambda$ and $\Delta\Gamma_{\mathbf{f}}$ denote the changes in eigenvalues (or equivalently natural frequencies) and mode shapes between the current structure and the initial model, respectively. Here, $i = 1, \ldots, p$ denotes the selected modal orders used in the calculation. The matrix $\mathbf{S}$ is the first-order sensitivity matrix assembling the sensitivities of the selected modal quantities with respect to the parameter vector α.

Due to inevitable measurement errors in frequencies and mode shapes, Equation (6) may not hold strictly. Therefore, it can be reformulated as

$$\mathbf{S}\boldsymbol{\alpha} - \Delta\Gamma = \varepsilon \tag{7}$$

where ε denotes the residual vector that collects modelling and measurement errors. The optimal parameter vector α^* is obtained by minimizing the residuals in Equation (7). Because modal frequencies and mode shapes are inevitably affected by field noise, and the inverse problem may be ill-conditioned, we introduce a Tikhonov regularization term ($\lambda\|\alpha\|^2$) and determine λ using the L-curve method [40]. Moreover, to reduce the risk of non-physical solutions that fit modal quantities but yield unrealistic structural responses, a weak prior constraint based on a representative displacement/response vector $\mathbf{\Gamma}_\alpha$ is included. When measured displacement data are available, $\mathbf{\Gamma}_\alpha$ can be constructed from the measurements; otherwise (as in the present case study) $\mathbf{\Gamma}_\alpha$ is taken from the baseline FE model as a weak prior. The resulting multi-indicator objective function is defined in Equation (8).

$$J(\boldsymbol{\alpha}) = \|\mathbf{S}\boldsymbol{\alpha} - \Delta\Gamma\|^{\ 2} + \lambda\|\boldsymbol{\alpha}\|^2 + \left\|\mathbf{\Gamma} - \mathbf{\Gamma}_a^i\right\|^2 \tag{8}$$

where λ is the regularization parameter and $\|\cdot\|_2$ denotes the Euclidean (L2) norm. In Equation (8), the first term enforces agreement with the modal residuals/sensitivity equation, the second term penalizes excessive parameter variation (regularization), and the third term introduces a weak prior constraint on the structural response. Specifically, $\mathbf{\Gamma}_a^i$ denotes the displacement/response vector computed from the updated model at the i-th iteration, whereas $\mathbf{\Gamma}_\alpha$ is the reference vector (taken from measurements when available, or from the baseline FE model as a weak prior). To prevent any single indicator from dominating due to different physical units and magnitudes, all residual vectors are converted to dimensionless form by normalization (e.g., by measured modal quantities), and weighting coefficients can be introduced when adapting the framework to other structures with different noise levels.

In the present case study, frequency residuals are normalized by the measured frequencies, and mode-shape agreement is quantified using the Modal Assurance Criterion (MAC) after consistent scaling of the measured and analytical mode vectors at the measured DOFs. Because the coefficients of variation (COV) of the identified modal frequencies are small, equal weights are adopted for the normalized modal indicators. When higher uncertainty is expected (e.g., strong ambient noise or fewer sensors), an inverse-variance weighting strategy ($w = 1/\sigma^2$) is recommended.

Equation (8) constitutes a comprehensive objective function, where the damage factor must satisfy all terms to minimize the objective function. This formulation is intended to improve the robustness of damage identification under sparse and noisy modal information.

2.2. Model Reduction

In structural damage identification, the large number of DOFs in a structure often exceeds the number of available sensors, resulting in modal data that only captures partial DOFs. To address this, it is necessary to reduce the model's DOFs to align with the measured data. The eigenvalue equation of the structure can be expressed in block form as follows:

$$\begin{bmatrix} \mathbf{K}_{mm} & \mathbf{K}_{mn} \\ \mathbf{K}_{nm} & \mathbf{K}_{nn} \end{bmatrix} \begin{bmatrix} \phi_m \\ \phi_n \end{bmatrix} = \omega^2 \begin{bmatrix} \mathbf{M}_{mm} & \mathbf{M}_{mn} \\ \mathbf{M}_{nm} & \mathbf{M}_{nn} \end{bmatrix} \begin{bmatrix} \phi_m \\ \phi_n \end{bmatrix} \tag{9}$$

where m and n denote the indices of the measured and unmeasured DOFs, respectively. ϕ_m and ϕ_n represent the measured and unmeasured parts of the i-th order mode shape ϕ_i, respectively. Let $m + n = N$. From the block eigenvalue equation, we obtain

$$\mathbf{K}_{mm}\phi_m + \mathbf{K}_{mn}\phi_n = \omega^2(\mathbf{M}_{mm}\phi_m + \mathbf{M}_{mn}\phi_n) \tag{10}$$

$$\mathbf{K}_{nm}\phi_m + \mathbf{K}_{nn}\phi_n = \omega^2(\mathbf{M}_{nm}\phi_m + \mathbf{M}_{nn}\phi_n) \tag{11}$$

To iteratively improve the model reduction techniques [41], the transformation matrix $\mathbf{T}_i$ is updated using the recursive formula:

$$\mathbf{T}_i = \mathbf{T}_{i-1} - \mathbf{T}_{i-1}\mathbf{M}_{nn}^{-1}(\mathbf{M}_{nm}\mathbf{T}_{i-1}) \tag{12}$$

where $\mathbf{T}_0 = \mathbf{I}$. Through iterative application of this formula, the stiffness matrix $\mathbf{K}_m$ and the mass matrix $\mathbf{M}_m$, corresponding to the measured DOFs m, can be expressed as

$$\mathbf{K}_m = \mathbf{T}_i^T\mathbf{K}\mathbf{T}_i \tag{13}$$

$$\mathbf{M}_m = \mathbf{T}_i^T\mathbf{M}\mathbf{T}_i \tag{14}$$

Similarly, the stiffness matrix $\mathbf{K}_{e_i}$ and the mass matrix $\mathbf{M}_{e_i}$ for the i-th element or region under the global DOFs N can be expressed as

$$\mathbf{K}_{e_i} = \mathbf{T}_i^T\mathbf{K}_e\mathbf{T}_i \tag{15}$$

$$\mathbf{M}_{e_i} = \mathbf{T}_i^T\mathbf{M}_e\mathbf{T}_i \tag{16}$$

In this study, the IRS refinement is performed with one iteration (i = 1). This choice reflects a trade-off between accuracy and efficiency: for the low-order modes of interest in building-scale SHM, IRS typically converges rapidly, and a single refinement already corrects the first-order condensation error introduced by the initial static (Guyan) reduction. Increasing j would increase computational cost and may amplify measurement noise in the reconstructed unmeasured DOFs. The condensed stiffness/mass matrices obtained with j = 1 are therefore adopted in the subsequent sensitivity and optimization calculations.

2.3. Mayfly Algorithm

The Mayfly Algorithm (MA) is an emerging swarm intelligence optimization technique designed to efficiently search for the minimum value of an objective function. As a population-based metaheuristic, MA provides a feasible global search strategy for the present inverse problem, but no general claim of superiority over other optimizers is made here. In this algorithm, mayflies are categorized into males and females, and through a series of social behaviors—such as flying, mating, and position adjustments—individuals dynamically adapt to achieve the optimization goal.

The social behavior of mayflies during courtship exhibits both individual and collective interactive characteristics. These behaviors are influenced not only by individual experiences but also by collective intelligence. When optimizing the damage coefficient, the position of a mayfly represents the degree of damage to structural elements, and the continuous updating of positions is guided by the sequence of social behaviors within the solution space.

At the outset of the optimization process, male and female mayflies are randomly generated and positioned within the problem space, forming an n-dimensional damage coefficient vector. The change in a mayfly's position is governed by its velocity $\mathbf{v} = (v_1, v_2, \ldots, v_n)$. Each mayfly adjusts its movement direction to move closer to its individual optimal position (p_{best}) and the overall optimal position (g_{best}).

In this context, the position of the i-th mayfly at time t is denoted as x_i^t, and its position at time $t + 1$ is updated as follows:

$$x_i^{t+1} = x_i^t + v_i^{t+1} \tag{17}$$

The velocity update for the male mayfly follows the formula:

$$v_{ij}^{t+1} = v_{ij}^t + c_1 e^{-\gamma d_p^2}(p_{\text{best}_{ij}} - x_{ij}^t) + c_2 e^{-\gamma d_g^2}(g_{\text{best}_j} - x_{ij}^t) \tag{18}$$

In this formula, v_{ij}^t represents the velocity of the i-th mayfly in the j-th dimension. c_1 and c_2 are positive attraction coefficients that quantify the influence of personal experience and social interactions, respectively. The parameter γ is a visibility factor that limits the observation range of the mayflies. The distance calculation can be expressed as

$$d_p = \|x_i - p_{\text{best}_i}\| = \sqrt{\sum_{j=1}^{n} (x_{ij} - p_{ij})^2} \tag{19}$$

To ensure that the best-performing mayflies in the colony maintain a moderate fluctuation in velocity, their speed can be updated using the following formula:

$$v_{ij}^{t+1} = v_{ij}^t + k \cdot r \tag{20}$$

where k is the dance coefficient, and r is a random value between -1 and 1. Female mayflies exhibit different behaviors compared to males, as their movement is directed towards the male mayflies. The process of updating their position can be expressed as

$$y_i^{t+1} = y_i^t + v_i^{t+1} \tag{21}$$

According to the criteria for mate selection, the female mayfly selects the healthiest male, and the formula for updating its velocity is as follows:

$$v_{ij}^{t+1} = \begin{cases} v_{ij}^t + c_2 e^{-\gamma d_m^2}(x_{ij}^t - y_{ij}^t) & \text{if } J(y_i) > J(x_i) \\ v_{ij}^t + f \cdot r & \text{if } J(y_i) \leq J(x_i) \end{cases} \tag{22}$$

where y_{ij}^t represents the position of the female mayfly, and d_m is the Cartesian distance between the female and male mayflies, which can be calculated using the formula. All mayflies generate offspring through mating, and the process is described as follows:

$$\begin{aligned} z_1 &= H \cdot m + (1 - H) \cdot fe \\ z_2 &= H \cdot fe + (1 - H) \cdot m \end{aligned} \tag{23}$$

In the above formulas, z_1 and z_2 represent the next generation of mayflies, m and fe denote the male and female parents, respectively, and H is a randomly generated value.

The basic steps for damage identification using the MA are as follows:

1. Determine the damage parameters and their ranges, and initialize the damage factor vector x, which represents the position of the mayfly.

2. Evaluate the objective function $J(x)$ for each candidate solution x (damage coefficient vector), and update the personal best (local optimum) of each mayfly as well as the population best (global optimum) solution gbest.
3. The position of male and female mayflies is updated to achieve adaptive adjustment of the damage coefficients. Mayflies will mate based on the principles of the MA, generating a new damage factor.
4. The newly generated damage coefficients are assigned to the male and female populations, and the objective function $J(x)$ is recalculated. Subsequently, the local optimal solution p_{best} and the global optimal solution g_{best} are updated.
5. Check the termination criteria. The optimization stops when the maximum number of iterations is reached or when the relative improvement of the best objective value over a prescribed window is smaller than a tolerance ε ($\varepsilon = 10^{-4}$ in this study). Otherwise, steps (3)–(5) are repeated.

In this manner, the MA can serve as a practical optimizer for the present inverse problem and provides a feasible search strategy for structural damage identification under sparse modal information.

Implementation details: In this study, the MA is implemented with equal numbers of male and female mayflies ($N_{\text{m}} = N_{\text{f}} = 25$), a maximum of 1000 iterations, inertia weight w = 0.7, attraction coefficients $c_1 = c_2 = 1.5$, dance coefficient $k = 0.1$, and flight coefficient fl = 0.1. Velocities are bounded to 20% of the parameter search range. These settings follow commonly used recommendations in the MA literature and provide a reasonable balance between exploration and exploitation. Because MA is a stochastic optimizer, independent runs with different random seeds can be performed and the best solution can be reported. Importantly, the proposed identification workflow is optimizer-agnostic and can be coupled with other metaheuristics (e.g., PSO, GA, CMA-ES) when required by a specific application. A supplementary optimizer benchmark on 24-dimensional test functions is provided in Appendix A.

2.4. Deep Learning Surrogate Model

When evaluating the objective function in Equation (8), commercial FE software (SAP2000 v26.1.0; Computers and Structures, Inc., Walnut Creek, CA, USA) must be repeatedly called to compute modal frequencies and mode shapes. For large buildings and high-dimensional updating, this repeated eigen-analysis becomes computationally expensive. Therefore, an efficient surrogate model that approximates the mapping from the updating parameters to the modal responses is introduced to accelerate the optimization process.

Deep learning, as a powerful machine learning technique, can directly establish complex mapping relationships between high-dimensional structural parameters and structural frequencies and mode shapes [42]. Consequently, this study employs a deep learning surrogate model to compute the frequency and mode shapes of the Christian Lutheran Church Building.

Under this framework, it is assumed that structural features can be characterized by a set of parameters $\boldsymbol{\alpha} = \{\alpha_1, \alpha_2, \ldots, \alpha_n\}^T$. Sample generation utilizes the Latin Hypercube Sampling (LHS) method, which involves constructing a one-dimensional uniformly distributed number of samples X. Each parameter is divided into X intervals, with each interval representing a sample. Random sampling is performed within each interval, and these samples are combined to generate sample points in X-dimensional space. The sample generation process can be represented by the following formula:

$$\alpha_i \sim \text{Uniform}(L_j, U_j),\ \forall j \in \{1,\ 2, \ldots,\ n\}\ (i = 1,\ 2, \ldots,\ X) \tag{24}$$

where L_j and U_j represent the lower and upper limits of the j-th parameter, respectively. A comprehensive representation of the samples can be presented through the following matrix, which contains all generated parameter samples:

For each generated parameter sample α_i, a frequency analysis is performed using FE software (SAP2000 v26.1.0) to calculate the corresponding eigenvalues λ_i and eigenvectors $\mathbf{f}_i$.

In this study, the specific steps for establishing a deep learning surrogate model for the Christian Lutheran Church Building are detailed as follows. First, the model is constructed with an input layer, multiple hidden layers, and an output layer. The input layer receives structural parameters related to the building, which effectively characterize the building's geometry and material properties. The hidden layers are designed as a multi-layered fully connected network, and the activation function uses ReLU (Rectified Linear Unit) to enhance the model's nonlinear representation capability. This helps capture the complex relationship between structural responses and input parameters. The output layer is used to predict the eigenvalues and eigenvectors of the building.

For reproducibility, the DNN surrogate model used in this study is a fully connected feed-forward neural network. The input dimension equals the number of updating parameters (24 in the case study). The output vector contains the first four natural frequencies and the corresponding mode-shape components at the measured DOFs, from which the MAC values are later computed. The 1000 LHS samples described in Section 3.5 are divided into 800 development samples and 200 independent test samples; within the development set, 10% are further reserved for validation during training. A five-layer architecture (256-256-128-128-64 neurons) with ReLU activations is adopted, and the output layer uses a linear activation. Inputs are normalized to [0, 1] based on the prescribed parameter bounds, and each output component is standardized using the mean and standard deviation of the training subset. The network parameters are estimated by minimizing the mean-squared error between the DNN predictions and the FE-computed modal quantities using the Adam optimizer with an initial learning rate of 1×10^{-3}, batch size of 32, and a maximum of 1000 epochs. To mitigate overfitting, early stopping (patience = 50 epochs), L2 weight decay (1×10^{-5}), and dropout (rate = 0.1) are applied.

Once trained, the surrogate model is evaluated in a forward pass that is computationally negligible compared with a full FE eigenvalue analysis. Therefore, within the optimization loop the DNN replaces most FE calls and the FE solver is only required for (i) generating the training dataset and (ii) occasional verification of the identified optimum. This provides an efficient trade-off between physics-based accuracy and computational cost.

During optimization, the trained DNN weights are kept fixed. If subsequent applications explore parameter regions outside the coverage of the original LHS samples, additional FE samples should be generated and the surrogate should be retrained before the identified solution is interpreted.

The mathematical expression of the model is

$$\mathbf{y} = \mathbf{NN}(\alpha; \theta) \tag{25}$$

where θ represents the model parameters, which are optimized during the training stage to improve prediction accuracy.

In model training, we employ the Mean Squared Error (MSE) as the loss function, which is defined as follows:

$$\mathcal{L}(\theta) = \frac{1}{N}\sum_{i=1}^{N}\left(\mathbf{y}_i^{\text{true}} - \mathbf{y}_i^{\text{pred}}\right)^2 \tag{26}$$

where $\mathbf{y}_i^{\text{true}}$ represents the true value of the i-th samples, and $\mathbf{y}_i^{\text{pred}}$ denotes the model's predicted value for the i-th samples. These parameters are used to calculate the prediction error, which evaluates the model's performance. Utilizing backpropagation algorithms and optimizers such as ADAM, the model parameters θ are iteratively updated during training to achieve optimal fitting.

After sufficient training, the model gains the capability to predict new samples. The prediction process is expressed as

$$\hat{\mathbf{y}} = \mathbf{NN}(\alpha_{new}; \theta) \tag{27}$$

Additionally, to validate the model's accuracy, we use the eigenvalues and eigenvectors of known samples to test the model and compute the correlation between predicted and actual results. The model's performance is evaluated using the coefficient of determination R^2, calculated as

$$R^2 = 1 - \frac{\sum_{i=1}^{N} \left(y_i^{\text{true}} - \hat{y}_i\right)^2}{\sum_{i=1}^{N} \left(y_i^{\text{true}} - \overline{y}\right)^2} \tag{28}$$

where $\overline{y}$ represents the mean of the true values. A deep learning surrogate model was established to perform FE analysis for the building, with specific parameter settings detailed in the subsequent example. The entire process of model construction, training, prediction, and validation is centered around the calculation of the building's frequencies and mode shapes, ensuring the model's effectiveness and accuracy.

This study introduces an integrated optimization framework for structural damage identification, merging multi-indicator objective functions, intelligent optimization algorithms, and deep learning to improve detection accuracy in complex structures. The methodology involves five key steps.

A multi-indicator objective function in Equations (1)–(8) is formulated using first-order sensitivity analysis to correlate structural eigenvalues with damage coefficients, enabling the holistic structural health evaluation. The residual minimization strategy in optimization incorporates Tikhonov regularization as shown in Equation (7) to mitigate the impact of measurement errors, thereby enhancing the robustness and reliability of the proposed method in practical applications.

Model reduction in Equations (9)–(14) addresses challenges posed by high DOFs and limited sensor coverage. The Iterative Refinement System (IRS) technique is utilized to efficiently align measured data with model predictions, thereby accelerating the optimization process, reducing computational time, and preserving result accuracy.

The MA method presented in Equations (17)–(23) optimizes damage identification by simulating individual and collective social behaviors. The mating and positional update mechanisms of mayflies increase the flexibility of damage factor adjustments, thus enhancing the probability of locating global optima. Furthermore, improvements in velocity and flexibility during the optimization process enable more effective handling of complex damage identification tasks.

A deep learning surrogate model, as described in Equations (25)–(27), substitutes for finite element analysis (FEA), thereby substantially decreasing computational expenses. The LHS method is employed to produce multi-dimensional samples, effectively capturing the intricate mapping relationships between structural parameters and dynamic responses. During the training phase of the model, the MSE serves as the loss function, and model parameters are optimized via backpropagation to improve prediction accuracy. The coeffi-

cient of determination, denoted as R^2, is utilized for model evaluation, thereby confirming its validity and performance.

Finally, the proposed methodology is applied to identify the operational state of the Christian Lutheran Church Building, with the goal of providing quantitative guidance for its assessment and rehabilitation based on the updated model. The case study illustrates the feasibility of the integrated workflow for high-dimensional parameter identification under sparse modal data.

2.5. Identifiability and Uncertainty Considerations

High-dimensional FE model updating can be ill-posed when the number of updating parameters is large relative to the amount and quality of measurement data. In the present framework, identifiability is improved by (i) grouping parameters by floor and component type (24 parameters in the case study, instead of element-wise updating), and (ii) jointly using modal frequencies and mode shapes at the measured DOFs as multiple indicators in the objective function. Although only the first four modal orders are used, each mode provides a scalar frequency and a spatial mode vector measured at 25 locations, which provides substantially more information than four scalar equations.

Regularization and weak prior constraints (Equation (8)) further reduce ill-conditioning by suppressing non-physical solutions and by mitigating the effect of field noise. The identified coefficients should be interpreted as effective stiffness-scaling factors of grouped components, reflecting both material degradation and modelling simplifications.

Even after parameter grouping, the inverse problem remains only partially identifiable. The practical objective is therefore to recover a physically plausible grouped stiffness pattern that reproduces the measured modal features, not to claim a mathematically unique parameter set. This interpretation is important when translating the identified coefficients into repair priorities. Accordingly, the present inversion should be regarded as an underdetermined problem, and the identified coefficients correspond to one admissible non-unique solution pattern rather than a single exact solution.

Uncertainty in the identified parameters arises from measurement noise, incomplete sensor coverage, modelling assumptions (e.g., reconstructed drawings and nominal material grades), and mode truncation. In this study, only a deterministic estimate is reported because the available field data are insufficient to support a stable probabilistic calibration. Accordingly, the 24 coefficients should be interpreted as effective grouped stiffness indicators rather than unique or fully identifiable physical constants. For applications requiring probabilistic outputs, the same workflow can be extended by (a) bootstrapping the measured modal data according to their estimated uncertainty and repeating the identification, (b) computing a linearized covariance estimate using the sensitivity matrix and an assumed measurement-noise covariance, or (c) embedding the grouped-parameter model in a Bayesian updating framework. These options are discussed here to define the current scope and to guide future applications. Hence, the identified parameters are non-unique solutions subject to uncertainty, not uniquely determined physical constants.

Finally, MAC values computed from sparse sensor layouts can be biased toward higher values. To mitigate this, MAC is evaluated only at the measured DOFs after consistent normalization of the measured and analytical mode vectors, and the objective function combines multiple indicators rather than relying on MAC alone. The overall condition-assessment workflow is summarized in Figure 1.

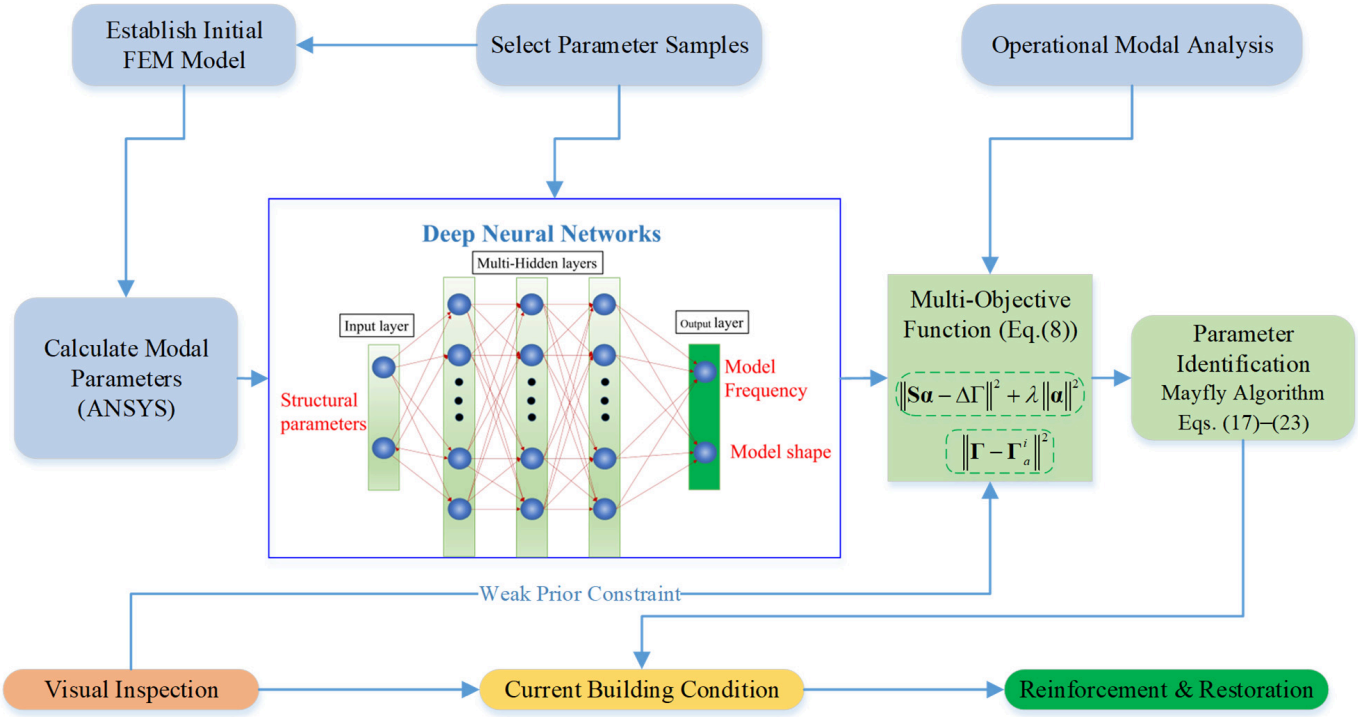


Figure 1. Structural condition assessment framework for the Christian Lutheran Church Building.

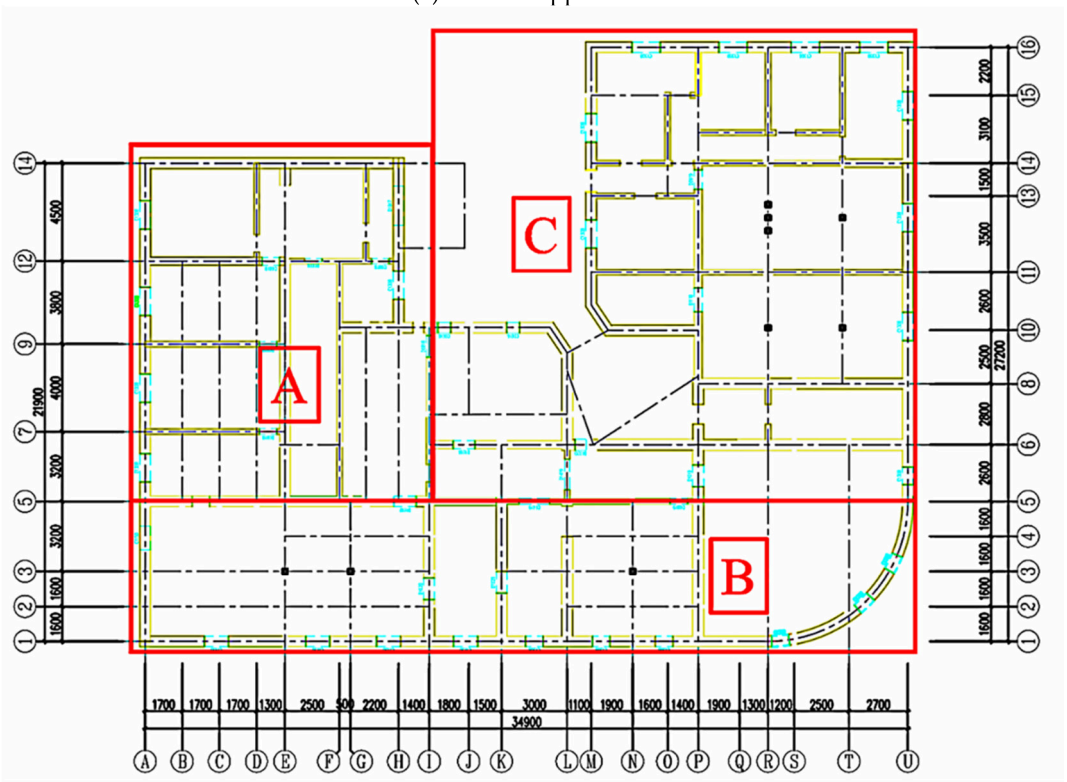
3. Case Study of the Christian Lutheran Church Building

The Christian Lutheran Church Building is a late classical style structure, originally constructed in 1923 and completed in 1924. The main building, finished in 1924, features a cast-in-place reinforced concrete frame structure, with walls constructed from fired clay bricks. The interior walls are 240 mm thick, while the exterior walls measure 490 mm in thickness. The floors consist of 200 mm thick cast-in-place concrete. The primary structure is a brick-concrete composite, with a total length of 32.56 m, a width of 28.40 m, and a total area of 5407.85 square meters. The basement has a height of 2.20 m, the first floor has a height of 4.20 m, and the second to fourth floors each have a height of 3.80 m. In the 1990s, two additional floors were constructed, featuring wooden floor slabs and a wooden roof structure. The heights of the fifth and sixth floors are 3.30 m and 3.00 m, respectively, with a sloped roof that is 1.50 m high. The total height of the building is 23.75 m. Figure 2a shows the exterior view of the building.

Due to the building's age, the original design drawings have been lost. A surveying agency conducted a re-evaluation of the building and reconstructed its original design drawings. The structural design is divided according to grid lines, as shown in Figure 2b. The structure is divided into three main areas: A, B, and C. Area A is defined by the grid lines of axes 5, 7, 9, 12, and 14, as well as the boundary grids on either side of axes A–I, which determine the locations of walls and structural nodes. Area B is controlled by the grid lines from axis 1 to axis 5 and the boundary grids on either side of axes A–U. Area C is defined by the grid lines from axis 5 to axis 16 and the boundary grids on either side of axes I–U. The bottom nodes are constrained with three-directional fixed supports to ensure the overall stability of the building.



(**a**) Exterior appearance

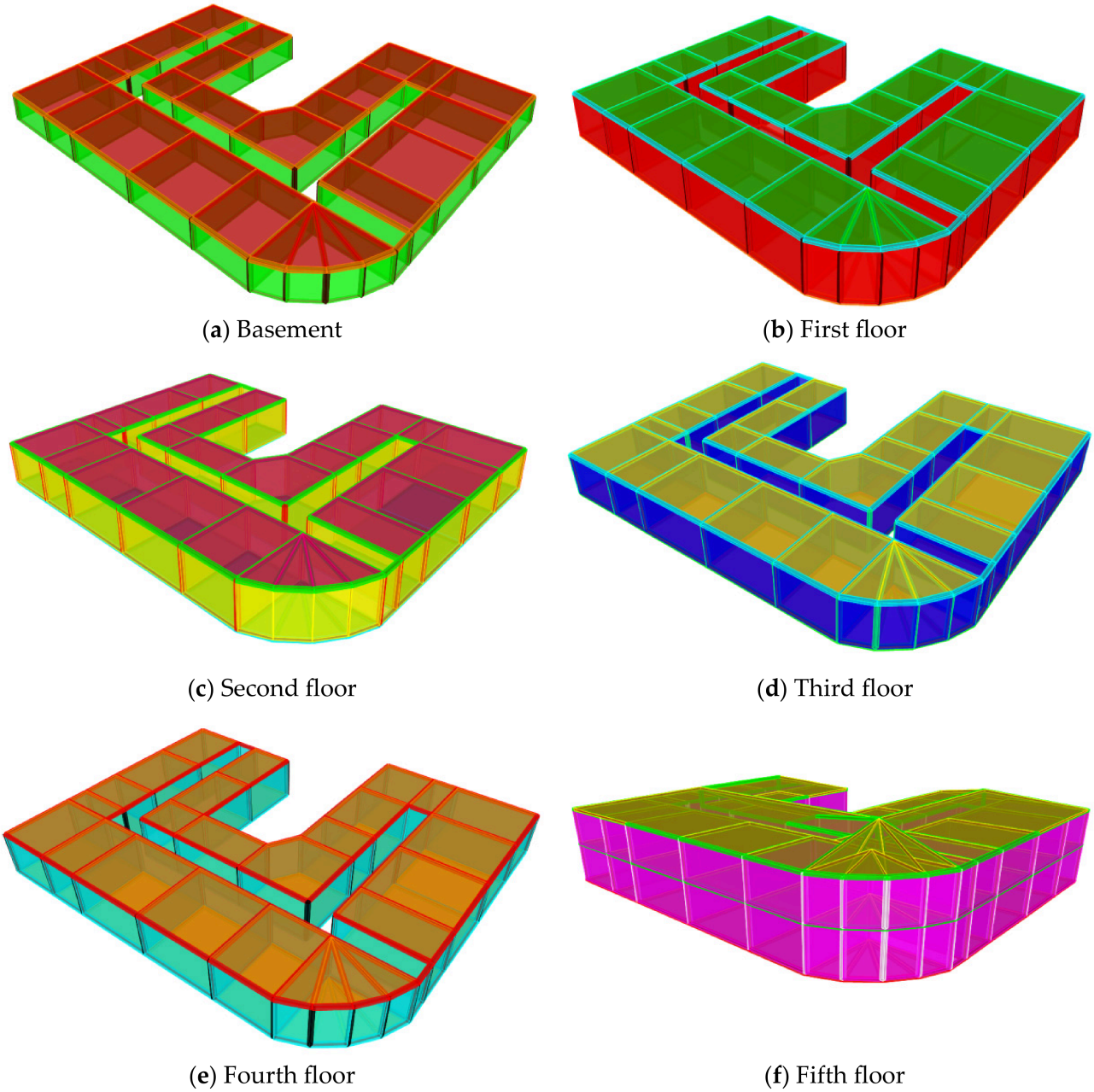


(**b**) Standard floor plan

Figure 2. The Christian Lutheran Church Building.

3.1. Initial FE Modeling of the Building

The initial FE model of the building was developed using SAP2000 structural analysis software, based on the obtained drawings. This model comprehensively considers all structural components, including columns, beams, floors, and walls. Figure 3 illustrates the detailed initial finite element model for each floor. Specifically, the column structure utilizes a total of 370 elements, while the beams consist of 575 elements, the floors include 195 elements, and the walls comprise 516 elements. Table 1 presents the material parameters for each structural component in the building model. Columns and beams are modeled using frame elements, whereas floors and partition walls are modeled using shell elements. The mass of each structural component is distributed based on assumed material densities, thereby constituting the self-weight of the components.



(**a**) Basement (**b**) First floor

(**c**) Second floor (**d**) Third floor

(**e**) Fourth floor (**f**) Fifth floor

Figure 3. FE model for each floor.

Table 1. Material properties of structural components.

Floor No.	Structural Element	Material Type	Properties of Materials	Modulus of Elasticity (Pa)	Section Size (m)
Basement to floor 4	Columns	Concrete	C15	1.2×10^{10}	0.25×0.25
	Beams	Concrete	C15	1.2×10^{10}	0.25×0.3
	Walls	Clay	MU10	2.72×10^{9}	/
	Slabs	Concrete	C15	1.2×10^{10}	0.2 (depth)
Floor 5 and 6	Columns	Concrete	C15	1.2×10^{10}	0.25×0.25
	Beams	Wood	-	7.0×10^{9}	0.25×0.3
	Walls	Clay	MU10	3.2×10^{9}	/
	Slabs	Wood	-	7.0×10^{9}	0.2 (depth)
Top floor	Columns	Wood	-	7.0×10^{9}	0.25×0.25
	Beams	Wood	-	7.0×10^{9}	0.25×0.3
	Slabs	Wood	-	7.0×10^{9}	0.2 (depth)

According to the Standard for Appraisal of Reliability of Industrial Buildings and Structures (GB 50144-2019) [43], the concrete used in buildings of that era typically employed ordinary Portland cement, corresponding roughly to the current C10–C20 grade. Therefore, in the preliminary model, the concrete strength is assumed to be C15. The strength of the fired clay bricks used within the building was evaluated through rebound testing, estimating the strength of the basement column components to be 14.9 MPa, while the strength of the first-floor beam components is estimated to be 12.3 MPa.

According to the Code for Design of Masonry Structures (GB 50003-2011) [44], the strength grade of ordinary fired bricks and fired hollow bricks used in masonry structures designed for a service life of 25 years or more should be M5. Field rebound tests were conducted to assess the strength of ordinary fired bricks in the building's columns, with test results indicating that the inferred brick strength grade from the basement walls to the sixth-floor walls is MU10. Additionally, a penetration-type mortar strength testing device was used to test the strength of the masonry mortar, revealing that the inferred mortar strength from the basement to the fourth-floor walls is 1.7 MPa. For bricks with a strength grade of MU10, the elastic modulus is calculated as $E = 1600 \times 1.70 = 2720$ MPa. The estimated mortar strength for the fifth and sixth-floor walls is 2.0 MPa, with a corresponding elastic modulus of $E = 1600 \times 2.0 = 3200$ MPa. The floors from the first to the fourth levels consist of 200 mm thick cast-in-place concrete slabs.

It is noteworthy that in 1990, two additional floors and a roof were added to the original structure, utilizing wooden floor slabs. The floor slabs are made of wood, and the roof trusses are constructed using wooden triangular trusses. According to preliminary survey reports, the wood used is oak. Given the relatively humid climate conditions in Wuhan, the initial elastic modulus of the wood is determined to be 7000 MPa. The roof features a four-sided sloped design, covered with red tiles, with certain areas designed as accessible rooftops. For the purposes of simulation analysis, the roof and the fifth and sixth floors are uniformly modeled as wooden structures. The final initial FE model of the entire building is illustrated in Figure 4.

It should be noted that to improve modeling efficiency and make reasonable use of computational resources, non-load-bearing structures such as doors, windows, and staircases were appropriately simplified during the model construction process; however, these simplifications did not significantly affect the overall accuracy and reliability of the model.

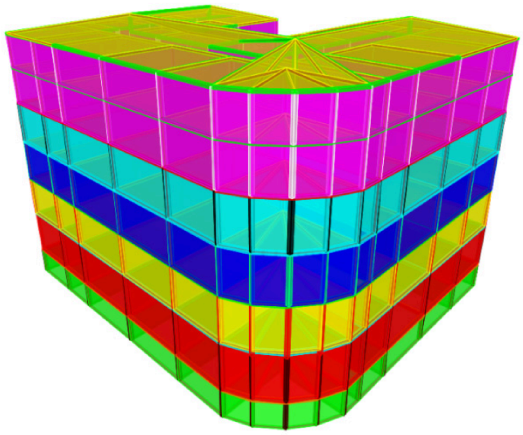
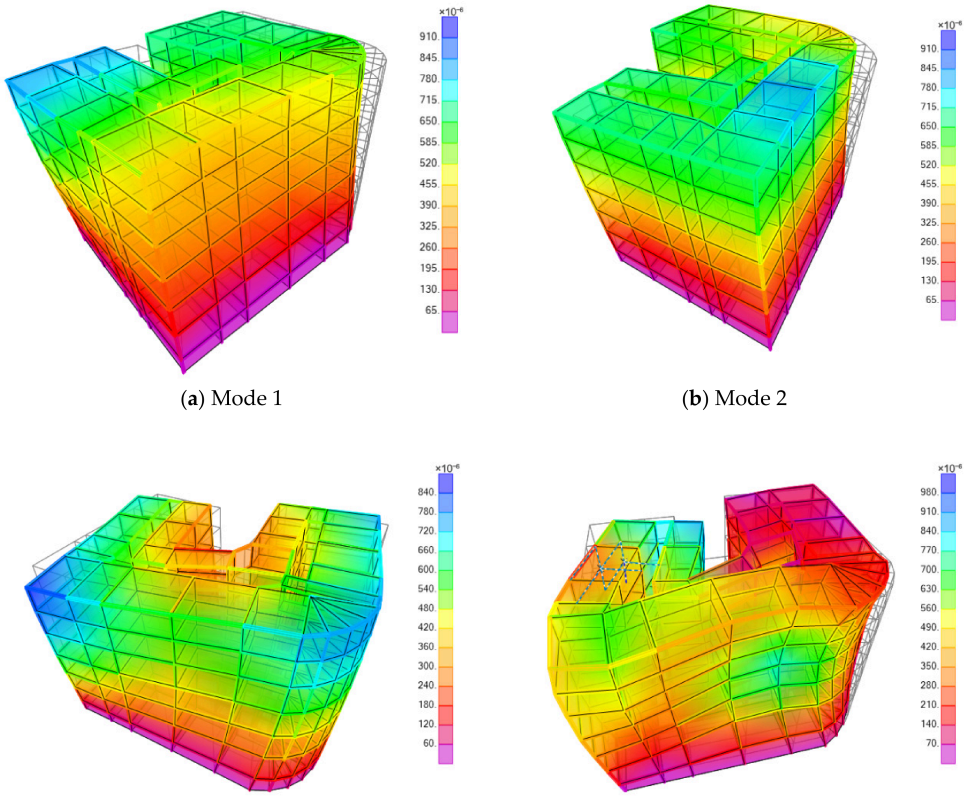


Figure 4. Overall FE model.

Following the establishment of the initial FE model of the building based on the design drawings, the first four modes of the structure were calculated using SAP2000 v26.1.0 structural analysis software, as illustrated in Figure 5. The first mode corresponds to a bending mode deflecting to the east, with a natural frequency of 4.66 Hz, as shown in Figure 5a. The second mode represents a bending mode deflecting to the south, with a natural frequency of 4.94 Hz, depicted in Figure 5b. The third and fourth modes are torsional modes, with natural frequencies of 6.873 Hz and 10.002 Hz, respectively, corresponding to the vibration modes shown in Figure 5c,d.



(**a**) Mode 1 (**b**) Mode 2

(**c**) Mode 3 (**d**) Mode 4

Figure 5. First four orders of modes of the initial model of the building.

3.2. Environmental Modal Test for the Christian Lutheran Church Building

To assess the actual condition of the Christian Lutheran Church Building and evaluate the extent of damage due to factors such as corrosion and fatigue, a modal test was conducted. Initially, based on the frequencies and mode shapes calculated from the FE model, it was determined that the building exhibits typical low-frequency vibration characteristics; therefore, low-frequency sensors were selected for the modal testing. The calculated mode shapes indicate that the first two modes are bending modes, while the third and fourth modes are torsional modes. Given the complexity of higher-order modes, the primary measurement objective was to capture the first four natural frequencies and their corresponding mode shapes of the building.

The testing equipment utilized was the Donghua dynamic data acquisition system. Based on the characteristics of the mode shapes calculated from the initial model, a sensor placement scheme was developed, as shown in Figure 6. A total of 25 acceleration measurement points were established. Five low-frequency accelerometers were used to collect acceleration signals in batches, with sensors B1 and D1 serving as reference points. The sampling frequency was set to 200 Hz. Among the five sensors, two were specifically positioned at the reference points and remained stationary. The other three sensors were moved in batches to collect data, resulting in a total of eight batches of acceleration signals, with each batch having a collection duration of no less than 10 min. The on-site testing setup and sensors are depicted in Figure 7.

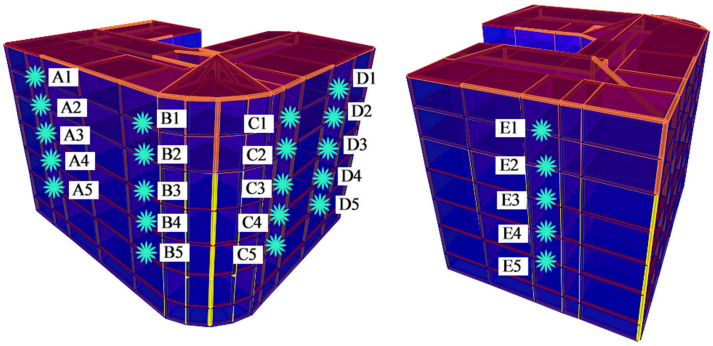


Figure 6. Layout of acceleration measurement points at the Christian Lutheran Church Building.

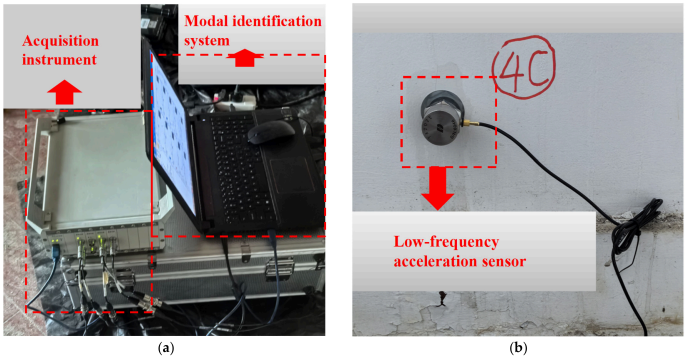


Figure 7. Acquisition systems and sensors: (**a**) Acquisition Instrument and modal identification system and (**b**) low-frequency acceleration sensor.

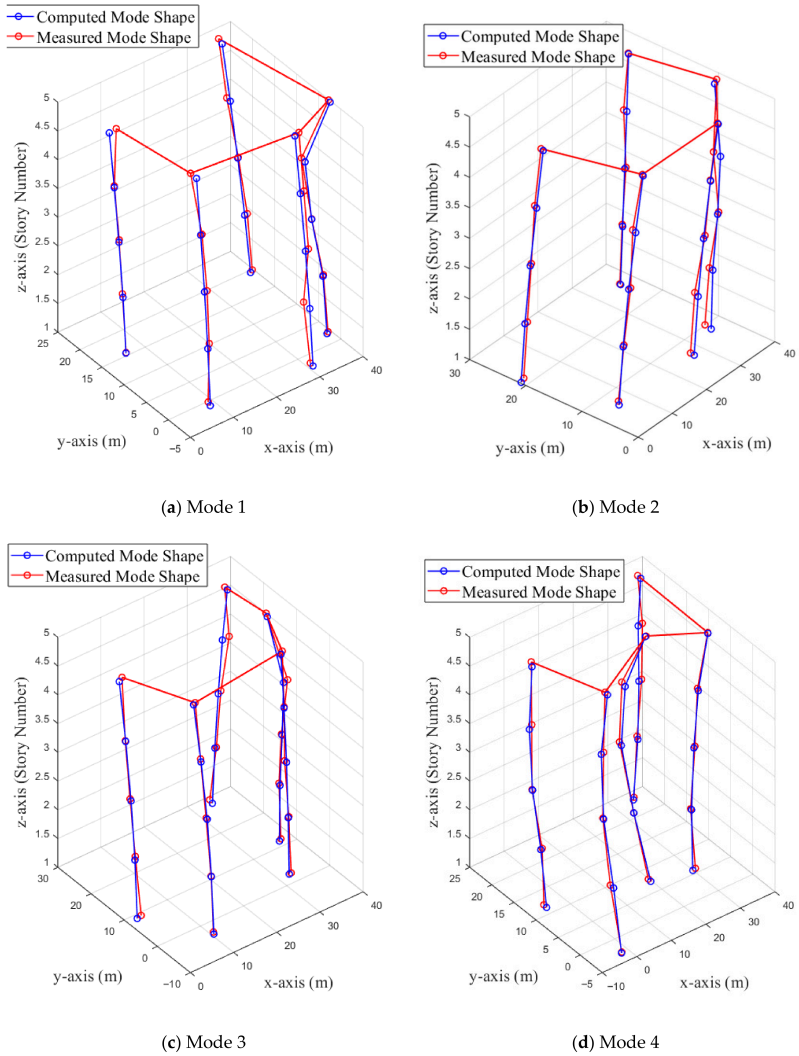
3.3. Modal Identification

The acceleration data obtained from the 25 measurement points were imported into the modal analysis system. The power spectral density method was employed to identify the inherent frequencies and mode shapes of the building. The measured frequencies of the first four modes are summarized in Table 2.

Table 2. The frequencies of the first four modes (Hz).

Modes	Initial	Measurement (Mean)	Measurement (COV)	Difference %
Vertical 1	4.66	2.539	0.004	−45.52%
Vertical 2	4.94	2.539	0.0038	−48.60%
Torsional 1	6.873	3.32	0.0021	−51.70%
Torsional 2	10.002	5.667	0.0034	−43.34%

As indicated in Table 2, the measured frequency of the first bending mode is 2.539 Hz, which represents a reduction of 45.52% compared to the initially calculated value of 4.66 Hz. Similarly, the measured frequency of the second bending mode is 2.539 Hz, showing a decrease of 48.60% from the initial calculation of 4.94 Hz. The first two bending modes constitute a closely spaced (near-degenerate) modal pair, which is common for structures with approximately symmetric stiffness distribution; under operational excitation and limited frequency resolution, their identified frequencies may appear identical, while the corresponding mode shapes remain distinguishable (Figure 8). The measured frequency of the third mode is 3.32 Hz (51.70% lower than the initial 6.873 Hz), and the measured frequency of the fourth torsional mode is 5.667 Hz (43.34% lower than the initial 10.002 Hz). The coefficients of variation for the measured frequencies of the first four modes are relatively small, indicating stable modal extraction.



(**a**) Mode 1 (**b**) Mode 2

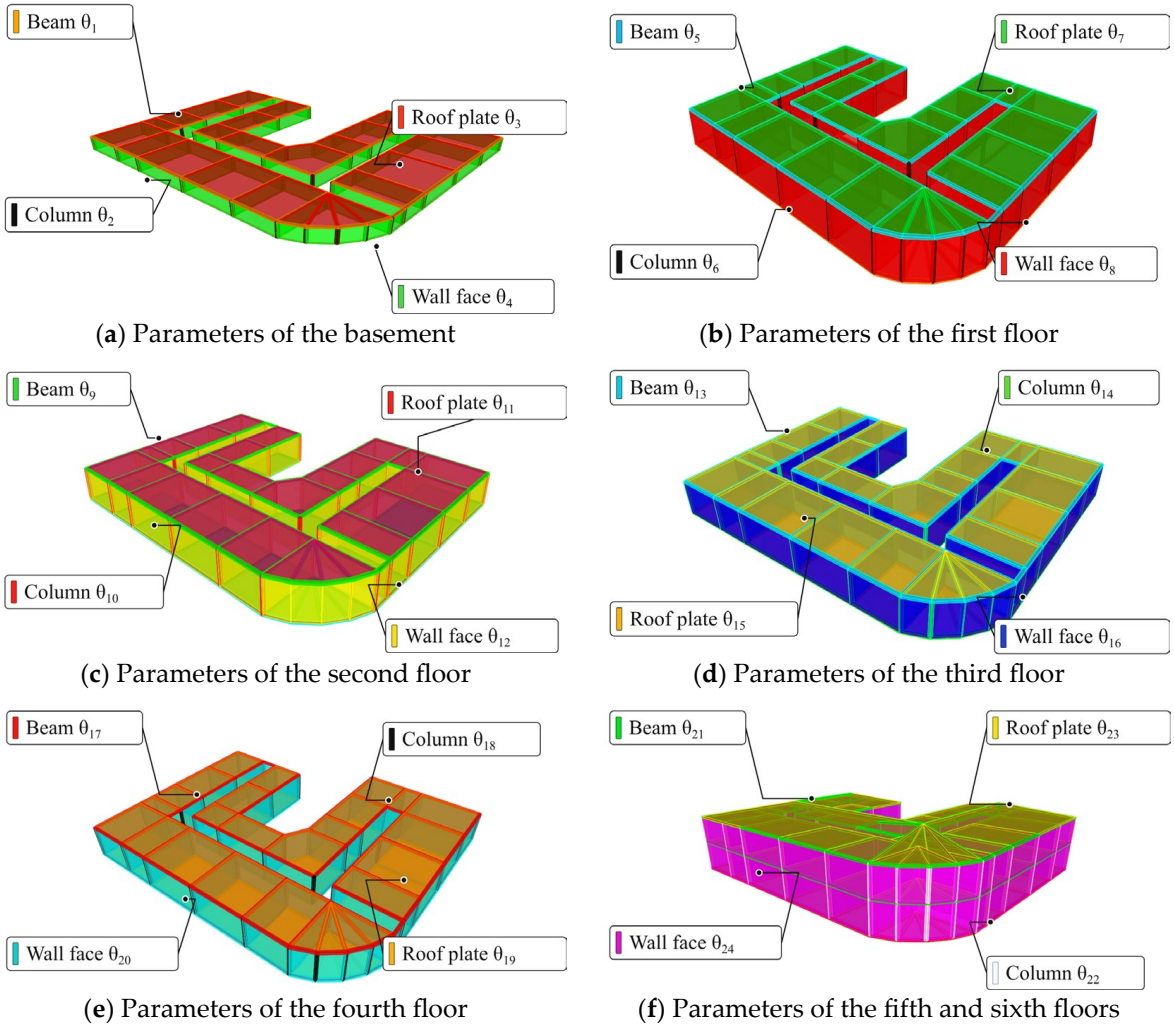
(**c**) Mode 3 (**d**) Mode 4

Figure 8. The first four measured mode shapes.

Based on the COV values in Table 2, the 95% confidence intervals of the measured frequencies are 2.519–2.559 Hz (Mode 1), 2.520–2.558 Hz (Mode 2), 3.306–3.334 Hz (Mode 3), and 5.629–5.705 Hz (Mode 4), indicating that the frequency-extraction uncertainty is below 1%. The corresponding measured mode shapes for the first four modes are presented in Figure 8. As observed from the measured modal shapes shown in Figure 8, although there is a general consistency with the initially calculated mode shapes, significant discrepancies are evident at the nodes. These subtle yet critical variations not only indicate potential damage within the building structure but also reveal a deeper degradation of the structural performance.

3.4. Selection of Parameters to Be Identified

To identify the current stiffness degradation of the Christian Lutheran Church Building and support rehabilitation planning, key updating parameters must be selected in a physically meaningful and identifiable manner. Based on on-site inspection, historical information, and the structural configuration, 24 grouped parameters (θ_1–θ_{24}) are defined. Each parameter represents an effective stiffness-scaling coefficient for one component type (columns, beams, walls, or slabs) at a given floor (Figure 9). Grouping reduces dimensionality compared with element-wise updating and improves both numerical stability and engineering interpretability.



(**a**) Parameters of the basement (**b**) Parameters of the first floor

(**c**) Parameters of the second floor (**d**) Parameters of the third floor

(**e**) Parameters of the fourth floor (**f**) Parameters of the fifth and sixth floors

Figure 9. Parameters to be identified.

3.4.1. Basement Parameters

1. The basement's structural integrity relies on four critical components:
2. Basement columns (θ_1) act as the primary load-bearing elements supporting the upper structures; they are therefore monitored as a key updating group to capture potential stiffness degradation.
3. Basement beams (θ_2) distribute loads across spans and strongly influence the global stiffness; they are included as an updating group to reflect deterioration of flexural and shear capacity.
4. Basement walls (θ_3) contribute to lateral stiffness and global stability; they are updated to reflect possible masonry degradation and cracking.
5. Basement slabs/floors (θ_4) connect the basement system and affect diaphragm action; they are included to capture stiffness changes due to damage or material ageing.

3.4.2. First Floor Parameterization

For the first floor, the grouped parameters are defined as: columns (θ_5), beams (θ_6), walls (θ_7), and slabs (θ_8). Because this level is directly connected to the ground and sustains substantial static and dynamic loads, these parameters are critical for the overall structural evaluation.

3.4.3. Second to Fourth Floors

The parameterization for the second to fourth floors follows the same grouping strategy to ensure consistency. Specifically, the second-floor parameters are columns (θ_9), beams (θ_{10}), walls (θ_{11}), and slabs (θ_{12}); the third-floor parameters are columns (θ_{13}), beams (θ_{14}), walls (θ_{15}), and slabs (θ_{16}); and the fourth-floor parameters are columns (θ_{17}), beams (θ_{18}), walls (θ_{19}), and slabs (θ_{20}). This unified selection facilitates floor-by-floor interpretation of stiffness degradation.

3.4.4. Fifth and Sixth Floors

For the newly added fifth and sixth floors with timber structural components, the grouped parameters are defined as columns (θ_{21}), beams (θ_{22}), walls (θ_{23}), and slabs (θ_{24}). This selection reflects the distinct mechanical properties of timber systems and the need to monitor time-dependent degradation mechanisms (e.g., moisture and biological effects).

In summary, the selection of these parameters prioritizes load-bearing functionality and floor-wise interpretability. To account for the different numerical magnitudes of material and sectional properties, the identification targets are defined as dimensionless coefficients. For reinforced-concrete columns, beams, and slabs, θ_k is defined as the relative change in elastic modulus with respect to its nominal value, i.e., $\theta_k = E/E_0 - 1$. For masonry walls, θ_k is defined as the relative change in the relevant masonry property (e.g., compressive strength or equivalent elastic modulus) with respect to its nominal value, $\theta_k = f/f_0 - 1$ (or $E/E_0 - 1$). Therefore, $1 + \theta_k$ represents the stiffness retention ratio. For example, $\theta_k = -0.5$ corresponds to a 50% reduction ($E = 0.5E_0$).

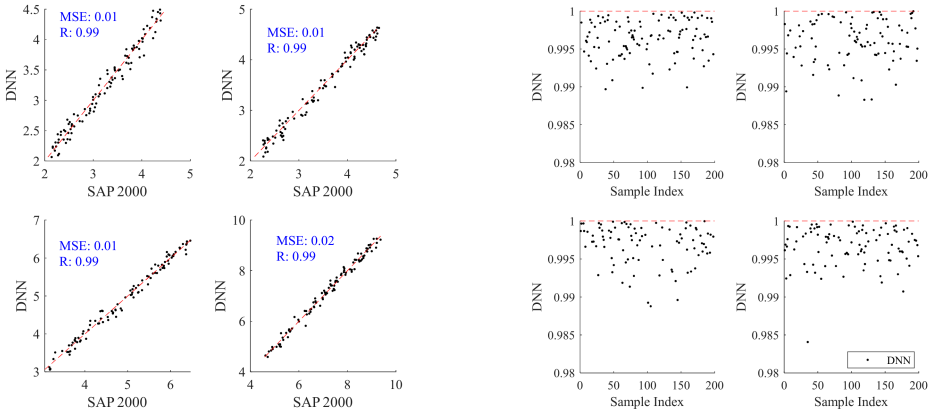
3.5. Parameter Identification

After selecting the parameters for identification, the LHS method was employed to generate 1000 sample sets for calculating the first four natural frequencies and mode shapes of the building. Given the significant reduction in measured frequencies and the findings from visual inspections, the parameter sampling range was set between $(-0.8, -0.2)$, indicating that the assumed damage level of the building ranges from -80% to -20%. The selected samples were input into the SAP2000 v26.1.0 software to compute the

corresponding first four mode shapes and frequencies for each sample set, with results normalized to the initial values.

The prior sampling range is further justified by the measured frequency drops. For building-scale systems with approximately constant mass, a reduction in stiffness generally leads to a decrease in natural frequency, following a square-root-type dependence between frequency and stiffness. Therefore, the globally retained stiffness can be estimated by taking the square of the ratio between the measured natural frequency and the corresponding initial-model frequency. Using the initial and measured frequencies in Table 2, the implied retention ratios for the first four modes are approximately 0.23–0.32, corresponding to about 68–77% stiffness loss at the global level. Accordingly, the adopted parameter range $(-0.8, -0.2)$ (i.e., retention ratio 0.2–0.8) covers the plausible degradation level while allowing for floor-wise and component-wise variation.

Using 800 of the sample sets, the DNN model was trained per Equation (27), while the remaining 200 sample sets were used to validate the accuracy of the surrogate model. Figure 10 compares the predicted responses of the surrogate model with the actual values. As shown in Figure 10a, the first four natural frequencies predicted by the DNN surrogate model closely match the results computed by SAP2000 v26.1.0. Figure 10b illustrates that the Modal Assurance Criteria (MAC) values predicted by the DNN are predominantly distributed between 0.985 and 1, indicating that the predicted mode shapes by the DNN are very similar to those computed by SAP2000 v26.1.0.



(**a**) Frequency (**b**) MAC

Figure 10. DNN-predicted frequencies and mode shapes.

These results indicate that the DNN surrogate can approximate the FE-predicted modal characteristics with high accuracy while significantly reducing evaluation cost, which is beneficial for accelerating high-dimensional parameter identification. The surrogate does not replace the physics-based FE model; instead, it serves as an efficient emulator within the optimization loop.

Next, the measured first four natural frequencies from Table 2 and the mode shapes from Figure 8 were substituted into Equation (8), and the proposed MA was employed for optimization. The optimization was terminated when either (i) the maximum number of iterations was reached (1000) or (ii) the relative improvement of the best objective value over the last 50 iterations was less than 10^{-4}. The search range for all parameters to be identified was set to $(-0.8, -0.2)$.

Figure 11 illustrates the evolution of the (normalized) objective function throughout the optimization process. After approximately 200 iterations, the objective value reaches a plateau and the relative improvement becomes very small. In the present run, the stopping condition was triggered by the maximum iteration limit (1000), with a final objective

value of 0.80. Because the objective function aggregates multiple normalized indicators, its absolute magnitude depends on the adopted scaling/weighting; therefore, the quality of the identified solution is primarily assessed by the achieved agreement between the updated and measured modal frequencies and mode shapes discussed later in this section.

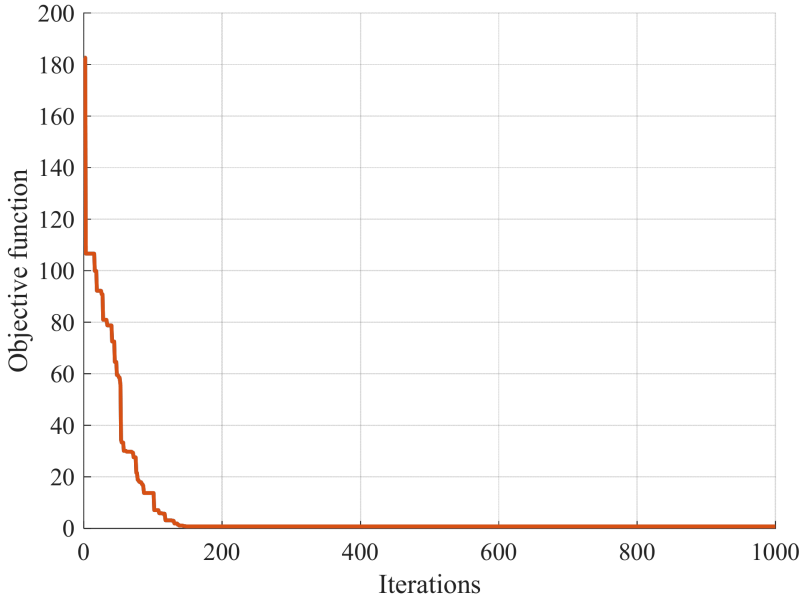


Figure 11. Loss function.

Figure 12 presents the identification results of all 24 grouped stiffness-reduction coefficients. The figure indicates comparatively large stiffness reductions—up to about 60%—primarily in the basement columns and beams and in the fourth-floor components. The columns and walls on the fifth and sixth floors also show notable reductions. By contrast, the basement walls and the first-floor beams and columns exhibit comparatively smaller reductions, around 40%.

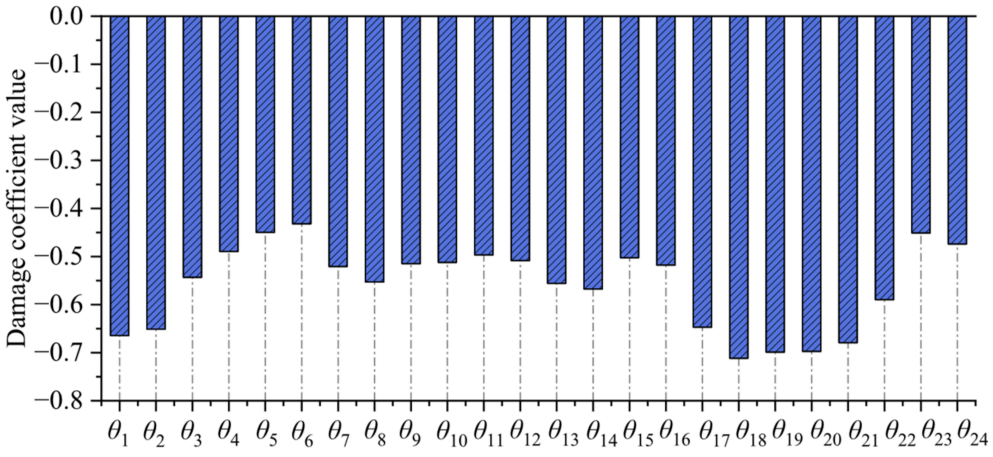


Figure 12. Identification results for 24 damage coefficients.

The grouped coefficients therefore provide a quantitative indication of relative stiffness reduction. Rather than replacing conventional visual inspection or direct material testing, they complement those methods by helping prioritize locations for detailed assessment and rehabilitation planning. Representative basement damage observations from the field inspection are shown in Figure 13.



Figure 13. Basement visualization results (some beams and columns). (**a**) Three-dimensional view of the basement (SAP model). (**b**) Severe rusting of secondary beams and peeling of concrete. (**c**) Severe deformation of the beam. (**d**) Main beams severely rusted with exposed rebar. (**e**) Column cracking. (**f**) Column damage. (**g**) Broken column with exposed reinforcement.

To further validate the accuracy of the identified results, the identified parameters were used as the current state parameters of the building to compute its current modal characteristics. Figure 14 compares the modal characteristics obtained from the current calculations with the initial values and measured values.

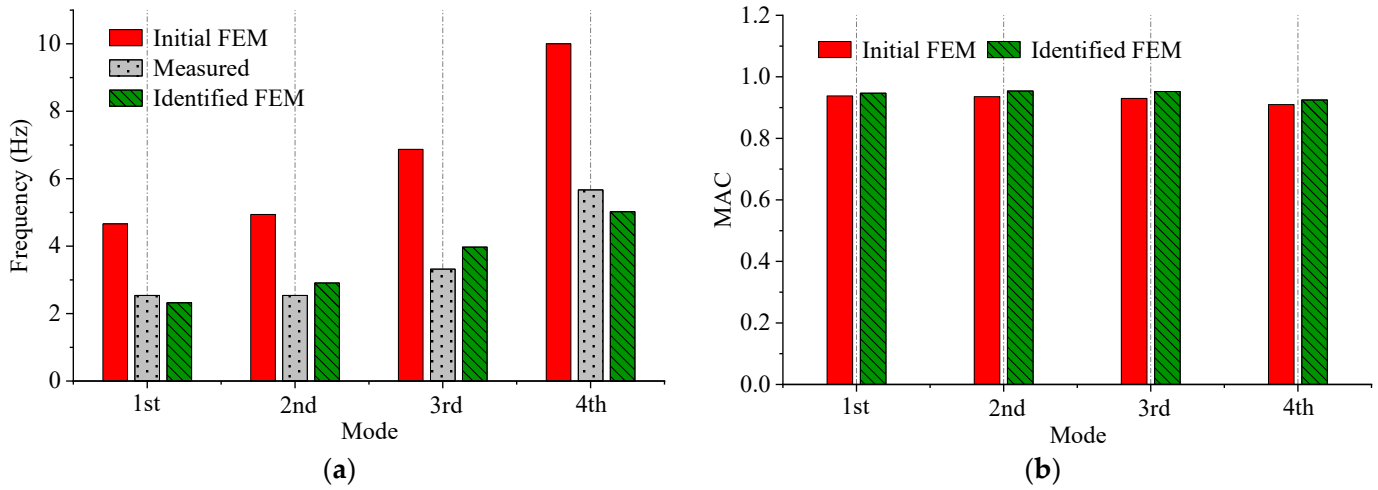


Figure 14. Comparison of modal properties in the current state. (**a**) Frequency comparison before and after identified. (**b**) Comparison of MAC before and after identified.

As shown in Figure 14a, there is a clear agreement between the response of the current state model and the measured values, indicating that the identified parameters can accurately replicate the current frequencies of the building. Furthermore, Figure 14b displays the MAC values between the computed modes and the measured mode shapes under the current state of the building. The results in Figure 14b clearly demonstrate that the calculated mode shapes are highly consistent with the measured mode shapes, further confirming that the identified parameters effectively characterize the current condition of the building. This provides a concrete basis for subsequent repair and reinforcement efforts.

3.6. Reinforcement Strategy

Based on the identified stiffness degradation, planning-level reinforcement measures are proposed to improve structural safety and serviceability. Following the local standard "Evaluation Criteria for Reinforcement Effects of Building Structures (DBJ51/T 131-2019)" [45], a target stiffness improvement of at least 20% is adopted as a quantitative intervention objective. These measures should be understood as candidate schemes derived from the updated model, rather than experimentally verified strengthening outcomes. The specific actions are as follows:

Heritage conservation considerations: For historical buildings, reinforcement should follow principles such as minimum intervention, compatibility of materials, and (when feasible) reversibility. Accordingly, the proposed measures aim to be as local and non-invasive as possible. For example, compatible repair mortars and bricks are preferred for masonry work. Techniques involving epoxy bonding or externally bonded FRP may have limited reversibility and should be carefully justified against conservation requirements; in practice they can be replaced or supplemented by more reversible alternatives (e.g., steel jacketing, mechanically anchored systems, or other removable strengthening details) when demanded by heritage authorities.

3.6.1. Repair of Key Load-Bearing Columns in the Basement ($\theta_1 = -0.69$)

The identified grouped coefficient for the basement columns suggests severe stiffness degradation, indicating that these members should be prioritized for detailed inspection and intervention design. Accordingly, a multi-level repair strategy is proposed at the planning stage:

1. Micro-damage repair using high-performance resin-based composite materials (e.g., epoxy resin and glass fiber) with micro-injection techniques may be considered to mend crack networks and restore the microscopic continuity of the concrete.
2. Subject to heritage-conservation approval, carbon-fiber wrapping technology may be considered to increase the effective thickness of the column cross-section and improve axial and shear capacity.
3. Prestressed anchoring with high-strength metal anchor points may also be considered at the base and other critical locations to improve stress-transfer paths and enhance overall structural stability, subject to detailed design verification.

These measures are proposed as planning-level design options intended to recover the stiffness and load-transfer capacity of the basement columns and to mitigate potential safety hazards. Their effectiveness should be verified through post-reinforcement numerical analysis and follow-up monitoring (see Section 3.7).

3.6.2. Systematic Repair of Beam Structures ($\theta_2 = -0.68$)

The grouped coefficient for the basement beams is also close to -0.7, indicating substantial stiffness degradation and the need for prioritized assessment. Accordingly, a comprehensive repair strategy can be considered.

1. High-strength stainless steel plates (yield strength $\geq$ 235 MPa) can be bonded to the bottom and sides of the beams using epoxy resin adhesive to enhance both flexural and shear performance.
2. High-modulus carbon fiber fabric can be introduced in the tensile regions of the beams via resin impregnation to form a collaborative strengthening system.
3. A carefully designed steel support structure can be introduced, with support points selected to improve the load-transfer path and mitigate local stress concentrations.

Overall, the identified damage distribution provides quantitative support for prioritizing reinforcement locations and selecting intervention measures. The updated model can serve as a baseline for post-reinforcement verification and long-term monitoring. In practice, the proposed measures should be refined based on detailed design constraints and, where possible, validated by post-intervention numerical reanalysis and/or follow-up modal testing. At this stage, these recommendations should be interpreted strictly as design proposals informed by the updated model, not as validated strengthening outcomes.

3.7. Post-Reinforcement Verification and Modal-Enhancement Check

The reinforcement target in this study is specified as a stiffness improvement of at least 20% according to DBJ51/T 131-2019 [45]. To improve engineering credibility, the proposed measures must be verified in two subsequent steps: (i) the FE model should be updated to reflect the designed interventions (e.g., increased sectional properties and/or material stiffness for strengthened members) and the modal properties should then be recalculated, and (ii) a follow-up ambient vibration test should be conducted after construction to confirm modal enhancement in the field. Because post-intervention measurements are not available at the current stage of the study, this section should be interpreted as a verification framework and analytical expectation only, not as direct proof that the proposed reinforcement has already achieved the claimed improvement.

For a structural system with approximately unchanged mass, the natural frequency scales with the square root of stiffness. Therefore, an overall 20% stiffness increase corresponds to an expected frequency increase of 1.095 (about 9.5%). Table 3 summarizes the corresponding frequency values for the first four measured modes as a reference for post-reinforcement assessment.

Table 3. Analytical frequency change corresponding to an overall 20% stiffness increase.

Mode	Measured Frequency (Hz)	Expected Frequency After +20% Stiffness (Hz)	Expected Increase (%)
1	2.539	2.781	9.5
2	2.539	2.781	9.5
3	3.320	3.637	9.5
4	5.667	6.208	9.5

4. Conclusions

This study presents an application-oriented workflow for modal-based FE model updating and rehabilitation planning for a historical building. By combining a multi-indicator objective function, the MA optimizer, and a DNN surrogate model, the case study demonstrates that grouped stiffness parameters can be estimated efficiently even when only sparse modal information is available.

For the Christian Lutheran Church Building, the updated model improves agreement with the measured modal frequencies and mode shapes and helps identify zones that warrant closer engineering attention, especially in the basement structural system. However, the reported coefficients should be interpreted as grouped effective indicators for diagnosis and prioritization, not as unique physical properties, and the proposed reinforcement measures remain planning-level recommendations until post-intervention simulation and field testing are completed. This interpretation is necessary because the present inverse problem remains underdetermined under the available sparse modal data.

The present study therefore provides a case demonstration of how established updating, optimization, and surrogate-modeling tools can be assembled for heritage-building decision support. It does not claim a direct performance benchmark against Bayesian updating or other probabilistic approaches, nor does it resolve uncertainty quantification within the current dataset. Future work will focus on uncertainty-aware updating, sensor-layout sensitivity, case-specific comparisons with alternative optimizers and Bayesian methods, and post-intervention validation.

Author Contributions: Conceptualization, Z.P. and B.C.; Data curation, Z.P., S.Z., Z.L. and W.L.; Formal analysis, Z.P. and S.Z.; Investigation, Z.P.; Methodology, Z.P., S.Z., Z.L. and W.L.; Project administration, Z.P., B.C. and S.Z.; Resources, Z.P.; Software, S.Z.; Supervision, B.C. and S.Z.; Validation, Z.P., B.C. and S.Z.; Writing—original draft, Z.P., B.C., S.Z., Z.L. and W.L.; Writing—review and editing, Z.P., B.C., S.Z. and Z.L. All authors have read and agreed to the published version of the manuscript.

Funding: This research was funded by the Special Research Project for Doctors of Wuhan City Polytechnic (grant number 2025WHCPB09). The APC was also funded by the Special Research Project for Doctors of Wuhan City Polytechnic.

Data Availability Statement: All data, models, and codes that support the findings of this study are available from the corresponding author upon reasonable request.

Conflicts of Interest: The authors declare no conflicts of interest. The funders had no role in the design of the study; in the collection, analysis, or interpretation of data; in the writing of this article; or in the decision to publish the results.

Appendix A. Optimizer Benchmark on 24-Dimensional Test Functions

In response to the reviewers' request for additional justification of the selected optimizer, a benchmark comparison is reported here for a 24-dimensional search space (matching the dimension of the case-study identification problem). The Mayfly Algorithm (MA) is compared with a standard Particle Swarm Optimization (PSO) implementation and

a basic Genetic Algorithm (GA) implementation on three commonly used test functions (Sphere, Rastrigin, and Ackley). For each function, all algorithms use the same population size (40) and iteration budget (300), and each experiment is repeated five times with different random seeds. The best objective value achieved in each run is recorded and the mean $\pm$ standard deviation is reported in Table A1. This benchmark does not replace a case-specific comparison on the structural objective function, but it provides evidence that MA is a competitive global search method in 24-dimensional spaces.

Table A1. Benchmark comparison of MA, PSO and GA on 24-dimensional test functions (best fitness; mean $\pm$ standard deviation over 5 runs).

Function	MA	PSO	GA
Sphere	$2.52 \times 10^{-5} \pm 1.5 \times 10^{-5}$	$1.53 \times 10^{-8} \pm 1.2 \times 10^{-8}$	0.629 ± 0.17
Rastrigin	116 ± 22	54.5 ± 13	75.6 ± 3.8
Ackley	0.312 ± 0.5	1.44 ± 1	5.64 ± 1.1

References

1. Nochebuena-Mora, E.; Mendes, N.; Lourenço, P.B.; Covas, J.A. Vibration control systems: A review of their application to historical unreinforced masonry buildings. *J. Build. Eng.* **2021**, *44*, 103333. [CrossRef]
2. Kouris, L.A.S.; Penna, A.; Magenes, G. Dynamic modification and damage propagation of a two-storey full-scale masonry building. *Adv. Civ. Eng.* **2019**, *2019*, 2396452. [CrossRef]
3. Farsangi, E.N.; Bogdanovic, A.; Rakicevic, Z.; Poposka, A.; Stojmanovska, M. Ambient vibration testings and field investigations of two historical buildings in Europe. *Struct. Durab. Health Monit.* **2020**, *14*, 283–301. [CrossRef]
4. Barontini, A.; Lourenço, P.B. Seismic safety assessment of mixed timber-masonry historical building: An example in Lima, Peru. *J. Earthq. Eng.* **2021**, *25*, 872–891. [CrossRef]
5. Rodríguez, A.S.; Rodríguez, B.R.; Rodríguez, M.S.; Sánchez, P.A. Laser scanning and its applications to damage detection and monitoring in masonry structures. In *Long Term Performance and Durability of Masonry Structures: Degradation Mechanisms, Health Monitoring, and Service Life Design*; Woodhead Publishing: Cambridge, UK, 2018; pp. 265–285. [CrossRef]
6. Anzani, A.; Garavaglia, E.; Binda, L. Long-term damage of historic masonry: A probabilistic model. *Constr. Build. Mater.* **2009**, *23*, 713–724. [CrossRef]
7. Asteris, P.G.; Chronopoulos, M.P.; Chrysostomou, C.Z.; Varum, H.; Plevris, V.; Kyriakides, N.; Silva, V. Seismic vulnerability assessment of historical masonry structural systems. *Eng. Struct.* **2014**, *62–63*, 118–134. [CrossRef]
8. Costantino, D.; Pepe, M.; Restuccia, A. Scan-to-HBIM for conservation and preservation of Cultural Heritage building: The case study of San Nicola in Montedoro church (Italy). *Appl. Geomat.* **2023**, *15*, 607–621. [CrossRef]
9. Tejedor, B.; Lucchi, E.; Bienvenido-Huertas, D.; Nardi, I. Non-destructive techniques (NDT) for the diagnosis of heritage buildings:tranditional procedures and furtures perspectives. *Energy Build.* **2022**, *263*, 112029. [CrossRef]
10. Işık, N.; Halifeoğlu, F.M.; İpek, S. Nondestructive testing techniques to evaluate the structural damage of historical city walls. *Constr. Build. Mater.* **2020**, *253*, 119228. [CrossRef]
11. Asad, M.; Thamboo, J.; Zahra, T.; Thambiratnam, D.P. Mitigating damages to infill walls under combined in-plane and out-of-plane loadings using a spider web-inspired strengthening strategy: Numerical analyses. *Eng. Struct.* **2025**, *323*, 119297. [CrossRef]
12. Salvalaggio, M.; Bernardo, V.; Lourenço, P.B. Exploring seismic fragility and strengthening of masonry built heritage in Lisbon (Portugal) via the Applied Element Method. *Eng. Struct.* **2024**, *320*, 118890. [CrossRef]
13. Braik, A.M.; Koliou, M. Automated building damage assessment and large-scale mapping by integrating satellite imagery, GIS, and deep learning. *Comput.-Aided Civ. Infrastruct. Eng.* **2024**, *39*, 2389–2404. [CrossRef]
14. Puertas, E.; Ávila, F.; García-Macías, E.; Gallego, R. Preventive preservation of rammed earth historical heritage through continuous monitoring, architectural inspections, and data fusion. *Buildings* **2024**, *14*, 3294. [CrossRef]
15. Huang, B.; Liu, X.; Liu, L.; Li, Z.; Wu, Z.; Huang, B.; Jia, Z. Unveiling the influencing factors of the residual life of historical buildings: A study of the Wuhan Lutheran Missions Home and Agency Building. *Buildings* **2025**, *15*, 246. [CrossRef]
16. Radnić, J.; Matešan, D.; Abaza, A. Restoration and strengthening of historical buildings: The example of Minceta Fortress in Dubrovnik. *Adv. Civ. Eng.* **2020**, *2020*, 8854397. [CrossRef]
17. Binda, L.; Saisi, A. Knowledge of the building, onsite investigation and connected problems. In Proceedings of the Workshop Eurocode 8 Perspectives from the Italian Standpoint, Naples, Italy, 3 April 2009; pp. 213–224.

18. Masciotta, M.G.; Ramos, L.F.; Lourenço, P.B. The importance of structural monitoring as a diagnosis and control tool in the restoration process of heritage structures: A case study in Portugal. *J. Cult. Herit.* **2017**, *27*, 36–47. [CrossRef]
19. Lourenço, P.B. Computations on historic masonry structures. *Prog. Struct. Eng. Mater.* **2002**, *4*, 301–319. [CrossRef]
20. Tsang, H.H. Innovative upscaling of architectural elements for strengthening building structures. *Sustainability* **2019**, *11*, 2636. [CrossRef]
21. Zeng, J.; Xue, K.; Chen, H. Real-time probabilistic model updating and damage detection using machine learning-based likelihood-free inference. *Mech. Syst. Signal Process.* **2025**, *230*, 112612. [CrossRef]
22. Martakis, P.; Reuland, Y.; Imesch, M.; Chatzi, E. Reducing uncertainty in seismic assessment of multiple masonry buildings based on monitored demolitions. *Bull. Earthq. Eng.* **2022**, *20*, 4441–4482. [CrossRef]
23. Li, L.; Liu, P.; Fu, J.; Yang, J. Vibration characteristics and seismic performance of historical buildings with brick-wood structures. *J. Vibroeng.* **2023**, *25*, 1547–1560. [CrossRef]
24. Chen, H.; Huang, B.; Zhang, H.; Xue, K.; Sun, M.; Wu, Z. An efficient Bayesian method with intrusive homotopy surrogate model for stochastic model updating. *Comput.-Aided Civ. Infrastruct. Eng.* **2024**, *39*, 2500–2516. [CrossRef]
25. Huang, B.; Xue, K.; Chen, H.; Sun, M.; Wu, Z. Stochastic static model updating of bridge using homotopy method and pre-estimated solution domain. *Struct. Control Health Monit.* **2025**, *2025*, 4714219. [CrossRef]
26. Zeng, Y.; Zeng, J.; Todd, M.D.; Hu, Z. Augmenting Bayesian inference-based damage diagnostics of miter gates based on image translation. In *Proceedings of the International Design Engineering Technical Conferences and Computers and Information in Engineering Conference, Washington, DC, USA, 25–28 August 2024*; American Society of Mechanical Engineers: New York, NY, USA, 2024; Volume 88360, p. V03AT03A041.
27. Zeng, J.; Todd, M.D.; Hu, Z. Dynamic state estimation via likelihood-free inference based on conditional invertible neural networks. In *Proceedings of the IMAC, A Conference and Exposition on Structural Dynamics, Orlando, FL, USA, 29 January–1 February 2024*; Springer: Cham, Switzerland, 2024; pp. 111–114.
28. Huang, B.; Chen, H. A new approach for stochastic model updating using the hybrid perturbation-Garlekin method. *Mech. Syst. Signal Process.* **2019**, *129*, 1–19. [CrossRef]
29. Wu, Z.; Huang, B.; Chen, H.; Zhang, H. A new homotopy approach for stochastic static model updating with large uncertain measurement errors. *Appl. Math. Model.* **2021**, *98*, 758–782. [CrossRef]
30. Zeng, J.; Todd, M.D.; Hu, Z. A recursive inference method based on invertible neural network for multi-level model updating using video monitoring data. *Mech. Syst. Signal Process.* **2023**, *203*, 110736. [CrossRef]
31. Zeng, J.; Todd, M.D.; Hu, Z. Probabilistic model updating for structural health monitoring using a likelihood-free Bayesian inference method. In *Proceedings of the Society for Experimental Mechanics Annual Conference and Exposition, Orlando, FL, USA, 5–8 June 2023*; Springer: Cham, Switzerland, 2023; pp. 123–125.
32. Song, M.; Yousefianmoghadam, S.; Mohammadi, M.E.; Moaveni, B.; Stavridis, A.; Wood, R.L. An application of finite element model updating for damage assessment of a two-story reinforced concrete building and comparison with lidar. *Struct. Health Monit.* **2018**, *17*, 1129–1150. [CrossRef]
33. Nozari, A.; Behmanesh, I.; Yousefianmoghadam, S.; Moaveni, B.; Stavridis, A. Effects of variability in ambient vibration data on model updating and damage identification of a 10-story building. *Eng. Struct.* **2017**, *151*, 540–553. [CrossRef]
34. Ramos, L.F.; Aguilar, R.; Lourenço, P.B.; Moreira, S. Dynamic structural health monitoring of Saint Torcato Church. *Mech. Syst. Signal Process.* **2013**, *35*, 1–15. [CrossRef]
35. Wu, G.; Yu, J.; Liu, X.; Jiang, X.; Ma, W.; Wang, S.; Liu, Y. Structural health detection and wind resistance safety assessment of ancient dwellings based on laser point cloud. *J. Build. Eng.* **2024**, *97*, 110816. [CrossRef]
36. Soleymani, A.; Jahangir, H.; Nehdi, M.L. Damage detection and monitoring in heritage masonry structures: Systematic review. *Constr. Build. Mater.* **2023**, *397*, 132402. [CrossRef]
37. Zervoudakis, K.; Tsafarakis, S. A mayfly optimization algorithm. *Comput. Ind. Eng.* **2020**, *145*, 106559. [CrossRef]
38. Wu, Z.; Song, Y.; Chen, H.; Huang, B.; Fan, J. A novel mayfly algorithm with response surface for static damage identification based on multiple indicators. *Int. J. Struct. Stab. Dyn.* **2024**, *24*, 2550071. [CrossRef]
39. Luo, Z.; Yu, L. Regularization strategies for contiguous and noncontiguous damage detection of structures. *Int. J. Comput. Methods* **2021**, *18*, 2140001. [CrossRef]
40. Zhang, C.D.; Xu, Y.L. Comparative studies on damage identification with Tikhonov regularization and sparse regularization. *Struct. Control Health Monit.* **2016**, *23*, 560–579. [CrossRef]
41. Friswell, M.I.; Garvey, S.D.; Penny, J.E.T. Model reduction using dynamic and iterated IRS techniques. *J. Sound Vib.* **1995**, *186*, 311–323. [CrossRef]
42. Sze, V.; Chen, Y.H.; Yang, T.J.; Emer, J.S. Efficient processing of deep neural networks: A tutorial and survey. *Proc. IEEE* **2017**, *105*, 2295–2329. [CrossRef]
43. *GB 50144-2019*; Standard for Appraisal of Reliability of Industrial Buildings and Structures. China Architecture & Building Press: Beijing, China, 2019.

44. *GB 50003-2011*; Code for Design of Masonry Structures. China Architecture & Building Press: Beijing, China, 2011.
45. *DBJ51/T 131-2019*; Evaluation Criteria for Reinforcement Effects of Building Structures. CCTC: Beijing, China, 2019.

Disclaimer/Publisher's Note: The statements, opinions and data contained in all publications are solely those of the individual author(s) and contributor(s) and not of MDPI and/or the editor(s). MDPI and/or the editor(s) disclaim responsibility for any injury to people or property resulting from any ideas, methods, instructions or products referred to in the content.